Valley surface-wave photonic crystal and its bulk/edge transport

Zhen Gao,[1] Zhaoju Yang,[1,*] Fei Gao,[1] Haoran Xue,[1] Yahui Yang,[1] Jianwen Dong,[2,†] and Baile Zhang[1,3,‡]

[1]*Division of Physics and Applied Physics, School of Physical and Mathematical Sciences,*
Nanyang Technological University, Singapore 637371, Singapore
[2]*School of Physics and State Key Laboratory of Optoelectronic Materials and Technologies,*
Sun Yat-Sen University, Guangzhou 510275, China
[3]*Centre for Disruptive Photonic Technologies, Nanyang Technological University, Singapore 637371, Singapore*

Recent theories have proposed a concept of valley photonic crystals as an analog of gapped valleytronic materials such as MoS_2 and bilayer graphene. Here, we further extend the applicability of valley photonic crystals to surface electromagnetic waves and experimentally demonstrate a valley surface-wave photonic crystal on a single metal surface as a photonic duplicate of MoS_2. Both bulk transport and edge transport are directly mapped with a near-field microwave imaging system. The photonic valley pseudospins are demonstrated, together with the photonic valley Hall effect that splits the opposite photonic valley pseudospins into two opposite directions. The valley edge transport in MoS_2 or other transition-metal dichalcogenide monolayers, which is different from bilayer graphene but still stays unrealized in condensed-matter systems, is demonstrated on this MoS_2-like photonic platform. Our study not only offers a tabletop platform to study the valleytronic physics, but also opens a venue for on-chip integrated photonic device applications using valley-polarized information.

The valley pseudospin, as a new degree of freedom (DOF) for electrons in two-dimensional (2D) transition-metal dichalcogenides (TMDCs) and bilayer graphene, has fueled remarkable research interest in the field of valleytronics [1–7], because of the exotic bulk and edge transport properties in these materials. For example, in the previously demonstrated valley Hall effect in MoS_2 [5], valley-polarized electrons move in opposite directions perpendicular to the drift current, as a result of the magnetic moment of a valley pseudospin that is proportional to the finite Berry curvature in momentum space [1,2]. When it comes to edge transport, although MoS_2 (and other TMDC monolayers) also hosts a valley-projected topological phase, topological valley edge transport so far has only been observed in bilayer graphene [6,7] at the domain wall between two valley-projected topological phases with opposite valley Chern indices [1,2]. The difference between MoS_2 and bilayer graphene is significant: The former carries *half-integer* valley-projected Chern numbers, while the latter hosts *integer* valley-projected Chern numbers, giving rise to different numbers of topological valley edge states (in the absence of spin DOF).

Being inspired by these exciting development in condensed matter systems, the concept of valley photonic crystals [8,9] has recently been proposed in the emerging field of topological photonics [10–18] to emulate the many valley-contrasting properties of valleytronic materials. In this Rapid Communication, we extend the concept of valley photonic crystals into surface electromagnetic waves, and demonstrate a valley surface-wave photonic crystal on a single metal surface, operating in the microwave regime. This valley surface-wave photonic crystal is a photonic duplicate of MoS_2 that possesses a staggered honeycomb lattice structure, providing a versatile

platform to study simultaneously the bulk and edge valley transport that is challenging in TMDC monolayers.

Our study is in the realm of spoof surface plasmons [19,20], or electromagnetic modes supported on periodically corrugated metal surfaces, with dispersions analogous to those surface plasmons at optical frequencies in metallic structures. These surface modes overcome the weak confinement of Zenneck surface waves, and hold considerable promise in microwave- to infrared-frequency device applications, because their properties can be fine tuned by simply altering the underlying structural parameters.

On this versatile platform of a valley surface-wave photonic crystal, we directly map the field distributions for bulk transport and edge transport, using a near-field microwave imaging system. In bulk transport, we demonstrate the existence of a photonic valley pseudospin, together with the photonic valley Hall effect that splits the opposite photonic valley pseudospins into two opposite directions, as an analog of the electronic valley Hall effect originally demonstrated in MoS_2 [5]. This photonic valley Hall effect is similar to the previous photonic spin Hall effect [21], where the two photonic spins (polarizations) are split into two opposite directions. In edge transport, we demonstrate that there is only *one* topological valley edge state per valley at a domain wall separating distinct valley topological phases in this MoS_2-like photonic system, as a result of the *half-integer* valley-projected Chern numbers as in TMDC monolayers. In contrast, a domain wall in bilayer graphene should support *two* topological valley edge states per valley. This supplements the incapability of condensed-matter experiments in demonstrating valley edge transport in TMDC monolayers.

Note that similar valley bulk and edge transport has been recently demonstrated for sound in an acoustic valley crystal [22–24]. Here, we focus on the electromagnetic system. Moreover, as explained in Ref. [23], this acoustic valley crystal adopts a "mirror-symmetry-breaking mechanism" based on the triangular shape of scatters, "instead of breaking the inversion
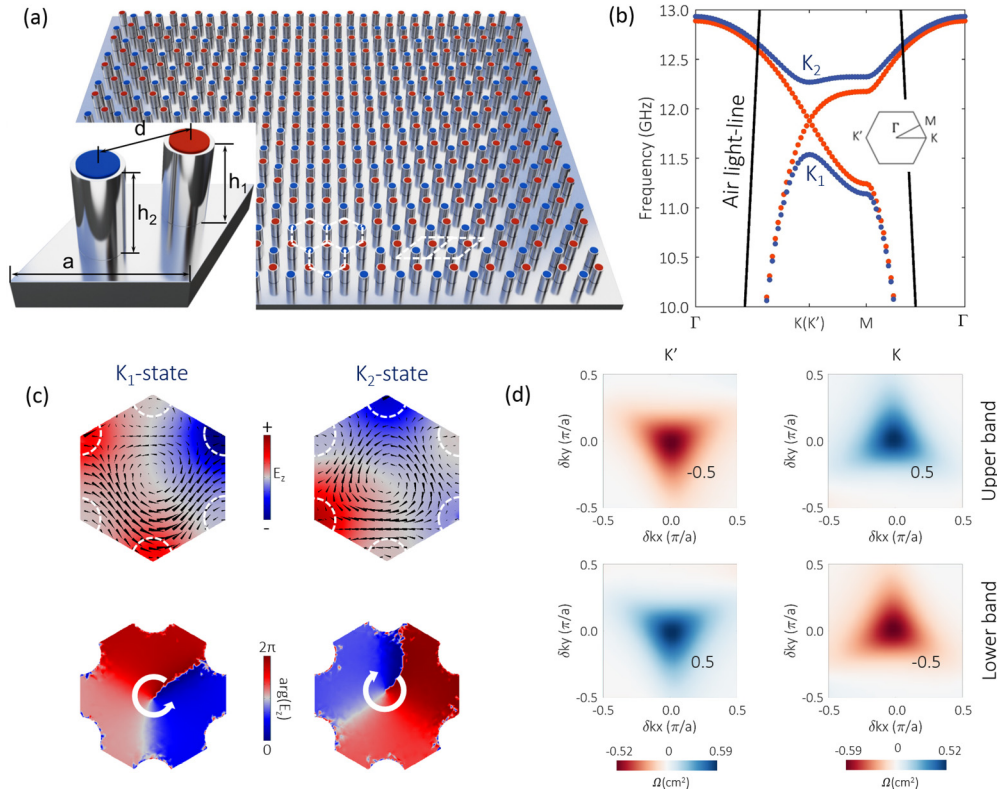

FIG. 1. Valley surface-wave photonic crystal and its bulk band structure. (a) Schematic of the crystal that has a graphene-like honeycomb lattice. A unit cell consists of two metallic rods standing on a metal surface with different heights. (b) Bulk band structures for the cases $\delta h = 0$ mm (red line) and $\delta h = 0.2$ mm (blue line). Black lines indicate the air light line. The inset shows the first Brillouin zone. (c) Upper: Simulated eigenmode profiles at the xy plane 1 mm above the taller rods. The black cones represent Poynting power flows. Lower: Simulated phase profiles at half height of taller rods. (d) Calculated Berry curvature near the K and K' valleys.

symmetry, as in graphene systems," and thus has no direct counterpart in either MoS$_2$ or other TMDC monolayers.

A schematic of the proposed valley surface-wave photonic crystal is shown in Fig. 1(a). It is a graphene-like honeycomb lattice of metallic rods with radius $r = 1.25$ mm standing on a metal surface. A rhomboid unit cell with lattice constant $a = 8.66$ mm, as illustrated in the lower left-hand corner, consists of two metallic rods with different heights separated by distance $d = 5$ mm. The shorter (marked in red) and taller (marked in blue) rods have heights of $h_1 = h_0 - \delta h = 4.6$ mm and $h_2 = h_0 + \delta h = 5$ mm, respectively, given that $h_0 = 4.8$ mm and $\delta h = 0.2$ mm. First, if we assume all rods have a uniform height $h_1 = h_2 = h_0 = 4.8$ mm (i.e., $\delta h = 0$), then the band diagram simulation (all simulations are performed with COMSOL MULTIPHYSICS) in Fig. 1(b) shows Dirac points at the K and K' corners of the Brillouin zone at a frequency of 11.9 GHz. Note that the valleys are located well below the air light line [black lines in Fig. 1(b)]; thus, the surface modes in the neighborhood of Dirac points can be supported on the surface-wave photonic crystal [25]. Then we turn on the height difference and set $\delta h = 0.2$ mm (i.e., $h_1 = 4.6$ mm and $h_2 = 5$ mm). This height difference plays the role of a staggered sublattice potential in MoS$_2$ [2,5]; it consequently breaks inversion symmetry and opens a complete band gap (11.5 GHz $< f <$ 12.3 GHz) at the original Dirac points (see the experimental demonstration of the band gap in the Supplemental Material [26]).

Take the split eigenstates [K_1 and K_2 in Fig. 1(b)] at K, for example. The simulated E_z fields at an xy plane 1 mm above the taller rods are plotted in the upper panel of Fig. 1(c). It can be seen that the electric fields mainly stay on top of the higher rods for the lower-energy eigenstate K_1, but shift to the shorter rods for the higher-energy eigenstate K_2. The Poynting vector rotates counterclockwise and clockwise for the K_1 and K_2 states, respectively. This kind of vortexlike rotation corresponds to the valley pseudospin in condensed-matter systems [1,2], or the orbital angular momentum of valley-polarized electrons, and thus can be termed as a photonic valley pseudospin. The chirality of a photonic valley pseudospin can be characterized by measuring the phase evolution [24]. The lower panel of Fig. 1(c) shows the phase profile at half height of the taller rods (i.e., at $h = 2.5$ mm), which exhibits clearly the counterclockwise and clockwise chirality. The eigenstates at the K' valley are time-reversal counterparts of the K_1 and K_2 states at the K valley.

The band topology of a valley surface-wave photonic crystal can be described by a massive Dirac Hamiltonian [9,10,23] $H = v_D(\delta k_x \sigma_x + \delta k_y \sigma_y) + m\sigma_z$. Here, v_D is the Dirac group velocity of the conical dispersion, $(\delta k_x, \delta k_y)$ is the momentum deviation from the $K(K')$ point, $\sigma_{x,y,z}$ are the Pauli matrices, and m is the effective mass induced by inversion-symmetry breaking of the rods with different heights. This Hamiltonian produces a nontrivial valley-dependent Berry curvature with a distribution sharply centered at the two valleys, as shown

in Fig. 1(d). Here, the Berry curvature can be calculated with $\Omega = \nabla_k \times \vec{A}(k)$, where $\vec{A}(k)$ is the Berry connection and $\nabla_k \equiv (\partial_{k_x}, \partial_{k_y})$. The Berry connection of the nth band is defined as $\vec{A}_n(k) = -i \langle u_k | \nabla_k | u_k \rangle$, where u_k is the normalized Bloch wave function that can be obtained through simulation. The numerical integration of Berry curvature near the $K(K')$ valley gives rise to the valley Chern index $C_{K(K')}$ that takes the values of $\pm \frac{1}{2}$, as indicated in each panel of Fig. 1(d). The integration of Berry curvature over the whole Brillouin zone is zero because of the time-reversal symmetry. Note that in this classical system, the Dirac Hamiltonian only helps to establish the analogy with semiconductor physics, while the only items necessary in calculation are the Bloch eigenfunctions, calculated from the COMSOL simulation.

Here, the sign of the effective mass m characterizes two different valley topological phases ($\delta h > 0$ and $\delta h < 0$) separated by a Dirac semimetal phase when $\delta h = 0$. Therefore, the topological transition of a valley surface-wave photonic crystal can be observed by tuning δh from positive to negative, and opposite photonic valley pseudospins at the K and K' valleys are inverted at $\delta h = 0$.

We have fabricated a valley surface-wave photonic crystal that is composed of aluminum rods standing on a flat aluminum surface, as shown in Fig. 2(a), following the design in Fig. 1(a) with $\delta h = 0.2$ mm. The width and length of the photonic crystal are 15 and 15 lattice constants, respectively. In the following, we first demonstrate the valley-chirality locked beam splitting, in which the separated beams are constructed by different valleys (K and K' valleys) and locked to the opposite chirality of the photonic valley pseudospin, as an analog of the valley Hall effect where valley-polarized electrons move in opposite directions perpendicular to the drift current.

A narrow incident beam that is generated with a waveguide-to-coaxial adapter (HD-100WCASKPA) is launched from the bottom of the photonic crystal, as schematically illustrated in Fig. 2(a). The forward moving states around the K and K' points (locked to the opposite photonic valley pseudospins) will move towards the opposite left and right directions. Figure 2(b) shows the experimentally observed field pattern at 11.3 GHz that was captured by a near-field microwave imaging probe scanning over the xy plane 1 mm above the taller rods of the photonic crystal. The two split beams are clearly observed. To identify the vortex chirality of a photonic valley pseudospin carried by the two split beams, we directly imaged the phase profiles of empty regions inside two unit cells that are located on the two beams, as shown in Fig. 2(b). A counterclockwise and clockwise phase evolution is evident for the left-moving (K valley) and right-moving (K' valley) beams, respectively. This valley-dependent beam splitting stems essentially from a trigonal warping effect of the band structure, where the isofrequency contours in momentum space tend to be of a trigonal shape, as shown in Fig. 2(c) at 11.3 GHz. Such a spatial separation of photonic valley pseudospins constitutes the photonic valley Hall effect, which is similar to the previous photonic spin Hall effect [21], where the two photonic spins (polarizations) are split into two opposite directions.

Now we proceed to demonstrate valley edge transport. As shown in Fig. 1(d), the integration of Berry curvature near the
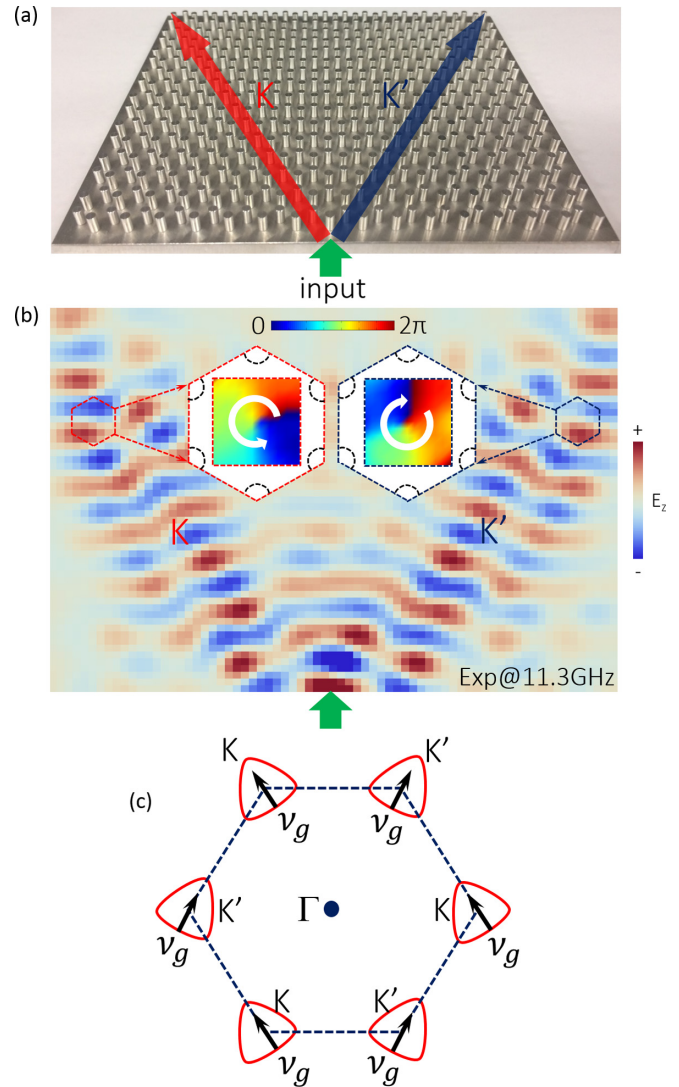

FIG. 2. Imaging photonic valley pseudospin and valley-Hall-like beam splitting. (a) Photograph of a fabricated valley surface-wave photonic crystal. The directions of valley-locked beam splitting are indicated with red and blue arrows. (b) The measured E_z field profile for a narrow beam incident normally from the bottom of the crystal at 11.3 GHz. The inset shows measured phase profiles inside two unit cells located on the left- and right-moving beams. (c) The trigonal-like isofrequency contours at 11.3 GHz. Directions of group velocity v_g are marked with arrows.

$K(K')$ valley for the lower band gives rise to the valley Chern indices $C_K = -1/2$ and $C_{K'} = 1/2$ for the valley surface-wave photonic crystal with $\delta h = 0.2$ mm. By changing δh from positive to negative, the valley surface-wave photonic crystal will experience a topological transition and flip the sign of the corresponding valley Chern indices. Therefore, for a domain wall separating distinct valley surface-wave photonic crystals with opposite half-integer valley Chern indices (which can be achieved by setting positive and negative values of δh), the difference in the valley-projected topological charges across the interface is quantized ($|\Delta C_K| = |C_K - C_{K'}| = 1$). This implies there should be *one* chiral edge state per valley propagating along the interface. Note that in bilayer graphene,
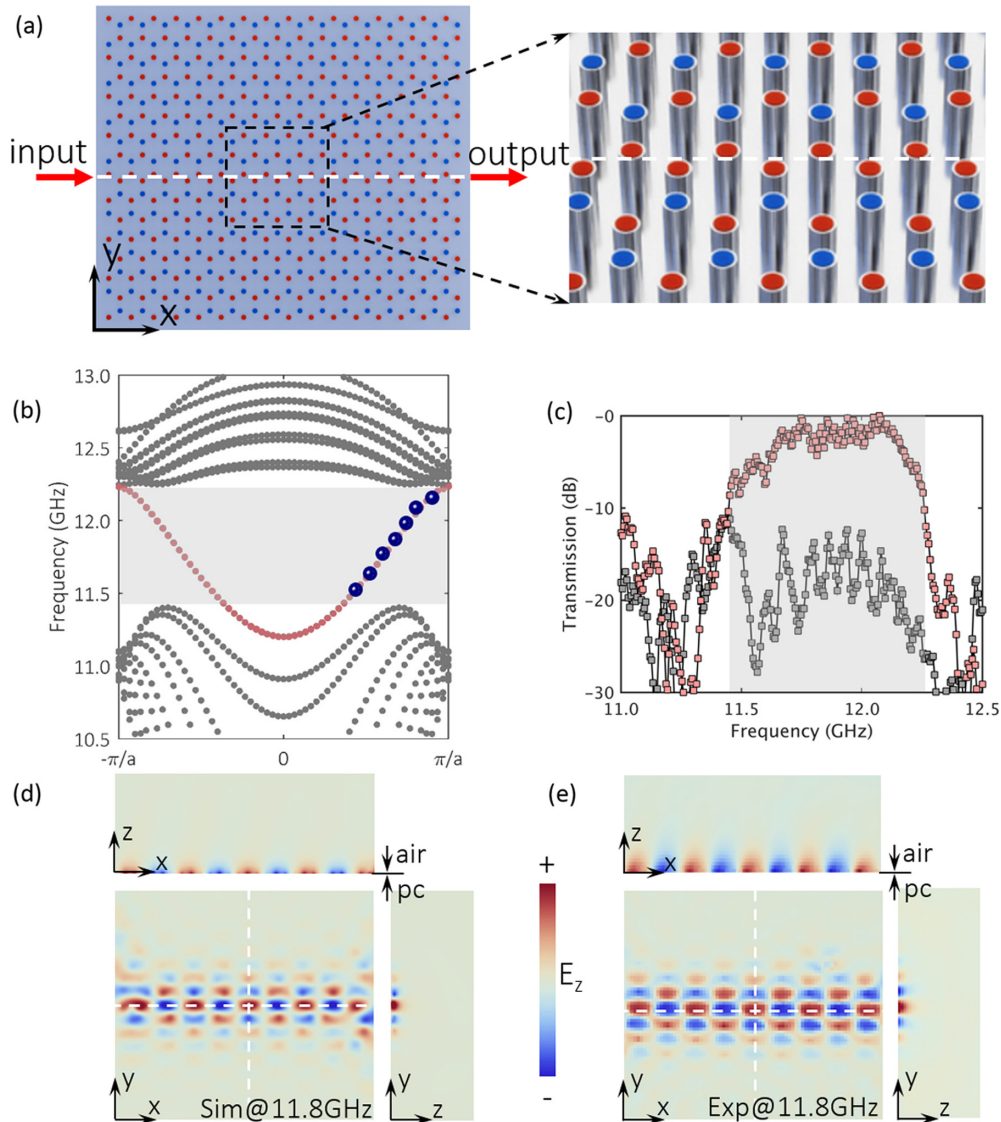
FIG. 3. Imaging valley edge states. (a) Schematic of a straight domain wall (dashed line) between the upper domain with $\delta h = 0.2$ mm and the lower domain with $\delta h = -0.2$ mm. (b) Dispersion of the valley edge states at the domain wall. The seven blue dots on the right branch of dispersion inside the band gap are obtained from Fourier transforming the mapped field patterns of valley edge states, similar to that in (e). (c) Measured transmission spectrum (red curve) along the domain wall. The transmission (gray curve) when the band gap in the upper domain closes was also measured for comparison. (d) Simulated and (e) imaged E_z field profiles in xy, xz, and yz planes at 11.8 GHz.

because of its integer valley Chern indices [$C_{K(K')} = \pm 1$], a bilayer-graphene domain wall separating valley topological phases with opposite valley Chern indices should have *two* chiral edge states ($|\Delta C_K| = 2$) per valley.

As shown in Fig. 3(a), we construct a domain wall between two valley surface-wave photonic crystals (the upper domain with $\delta h = 0.2$ mm and the lower domain with $\delta h = -0.2$ mm) with opposite half-integer valley Chern indices. All rods at the domain wall are the shorter rods with height 4.6 mm. The band diagram simulated in Fig. 3(b) shows that there are valley-polarized topological edge states (red line) in the band gap at the domain wall, whose propagating directions are locked to the K and K' valleys. The gray lines in Fig. 3(b) correspond to the bulk states.

A vertical monopole antenna was placed at the left end of the domain wall to excite the valley-polarized edge states.

Another monopole antenna at the right end of the domain wall was used to measure the transmission spectrum. The measured transmission band of the valley edge states [red line in Fig. 3(c)] matches well with the frequency range of their calculated dispersion [red line in Fig. 3(b)]. The imaged field patterns of the valley edge state at the K valley in the xy, xz, and yz planes at 11.8 GHz [Fig. 3(e)] match with the simulated ones [Fig. 3(d)], demonstrating that the edge states are evanescently decayed and well confined at the domain well in both the vertical and transvers directions. Note that the topological edge states will disappear if the band gap at one domain is closed. By replacing all taller rods in the upper domain with shorter rods, the transmission drops dramatically in the measurement [gray line in Fig. 3(c)].

By Fourier transforming the mapped field pattern in Fig. 3(e) along the domain wall, we can obtain the wave vector
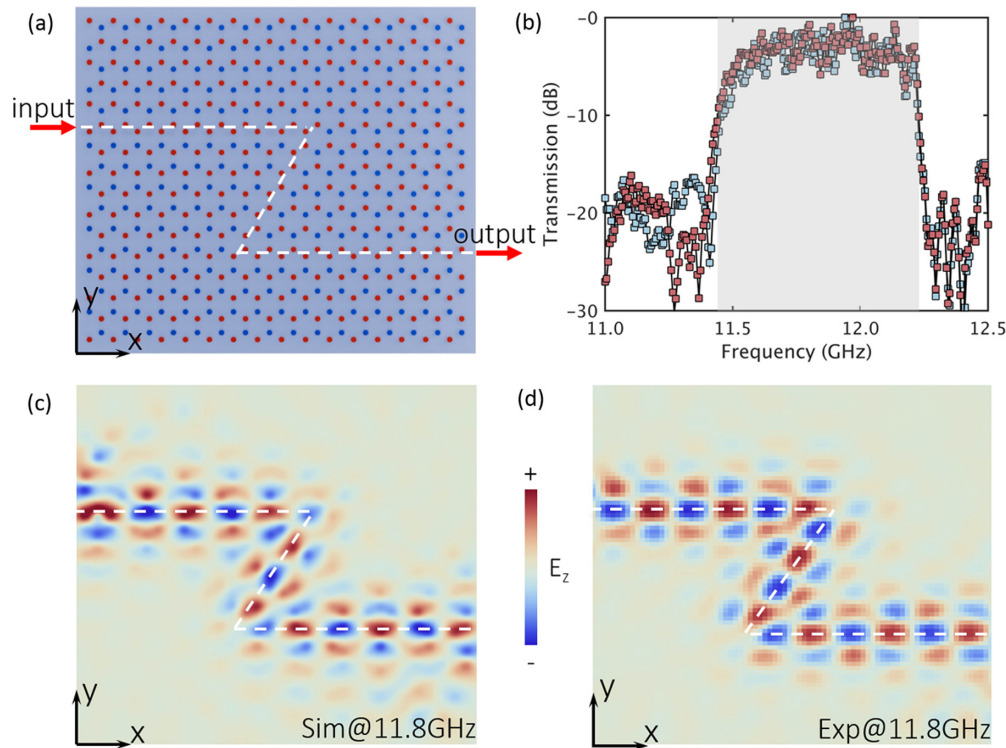
FIG. 4. Robustness of topological valley edge states. (a) Schematic of the zigzag domain wall (dashed line) between the upper domain with $\delta h = 0.2$ mm and the lower domain with $\delta h = -0.2$ mm. (b) Comparison of measured transmittance along a straight domain wall (dark red line) and a zigzag domain wall (green line) for the topological valley edge states. (c) Simulated and (d) imaged E_z field profiles in the xy plane 1 mm above the sample at 11.8 GHz.

for the valley edge state at 11.8 GHz. Repeating this process at seven different frequencies, we can obtain the dispersion of the valley edge states at the K valley spanning the whole band gap, as shown by the seven blue dots in Fig. 3(b). The other half branch of dispersion at the K' valley can be obtained by time-reversal symmetry. This clearly shows that there is only *one* topological valley edge state per valley in this MoS$_2$-like system.

For completeness, we then construct a zigzag path for the domain wall, as shown in Fig. 4(a), to demonstrate robust valley edge transport in the absence of intervalley scattering. The measured transmission [green line in Fig. 4(b)] shows negligible suppression inside the band gap, and is almost identical to the transmission [dark red line in Fig. 4(b)] along a straight domain wall with the same length. We then mapped the E_z field pattern at 11.8 GHz, as shown in Fig. 4(d), which matches well with the simulation in Fig. 4(c). Both Figs. 4(c) and 4(d) show that the topological valley edge state can be guided around the zigzag path smoothly without reflection.

In conclusion, we have extended the concept of valley photonic crystals to surface electromagnetic waves, and demonstrated a valley surface-wave photonic crystal on a single metal surface as a photonic duplicate of MoS$_2$. By mapping the valley-polarized vortex states, the existence of a photonic valley pseudospin is demonstrated, together

with the photonic valley Hall effect that splits the opposite photonic valley pseudospins into two opposite directions. The topological valley edge state at a domain wall in MoS$_2$ or other TMDC monolayers, which has not been constructed in condensed-matter systems, has been demonstrated in this MoS$_2$-like photonic system. Our work may open up a route to device applications of photonic valleytronics on the platform of integrated plasmonic circuits.

Note added. Recently, we became aware of independent work [27] on imaging valley edge states on a designer surface plasmon crystal. Another work [28] reports valley edge states at optical frequencies. Reference [29] reports on the perfect outcoupling of valley edge states designed from a spin-compatible four-band model. The main conclusions in the current Rapid Communication are still valid.

[1] D. Xiao, W. Yao, and Q. Niu, Phys. Rev. Lett. **99**, 236809 (2007).

[2] X. Xu, W. Yao, D. Xiao, and T. F. Heinz, Nat. Phys. **10**, 343 (2014).

[3] G. W. Semenoff, V. Semenoff, and F. Zhou, Phys. Rev. Lett. **101**, 087204 (2008).

[4] I. Martin, Y. M. Blanter, and A. F. Morpurgo, Phys. Rev. Lett. **100**, 036804 (2008).

[5] K. F. Mak, K. L. McGill, J. Park, and P. L. McEuen, Science **344**, 1489 (2014).

[6] L. Ju, Z. Shi, N. Nair, Y. Lv, C. Jin, J. Velasco, Jr., C. Ojeda-Aristizabal, H. A. Bechtel, M. C. Martin, A. Zettl, J. Analytis, and F. Wang, Nature (London) **520**, 650 (2015).

[7] J. Li, K. Wang, K. J. McFaul, Z. Zern, Y. Ren, K. Watanabe, T. Taniguchi, Z. Qiao, and J. Zhu, Nat. Nanotechnol. **11**, 1060 (2016).

[8] T. Ma and G. Shvets, New J. Phys. **18**, 025012 (2016).

[9] J. Dong, X. Chen, H. Zhu, Y. Wang, and X. Zhang, Nat. Mater. **16**, 298 (2017).

[10] Z. Wang, Y. Chong, J. D. Joannopoulos, and M. Soljacic, Nature (London) **461**, 772 (2009).

[11] M. C. Rechtsman, J. M. Zeuner, Y. Plotnik, Y. Lumer, D. Podolsky, F. Dreisow, S. Nolte, M. Segev, and A. Szameit, Nature (London) **496**, 196 (2013).

[12] M. Hafezi, S. Mittal, J. Fan, A. Migdall, and J. M. Taylor, Nat. Photon. **7**, 1001 (2013).

[13] A. B. Khanikaev, S. H. Mousavi, W. Tse, M. Kargarian, A. H. MacDonald, and G. Shvets, Nat. Mater. **12**, 233 (2013).

[14] L. Lu, J. D. Joannopoulos, and M. Soljacic, Nat. Photon. **8**, 821 (2014).

[15] W. Chen, S. Jiang, X. Chen, B. Zhu, L. Zhou, J. Dong, and C. T. Chan, Nat. Commun. **5**, 5782 (2014).

[16] F. Gao, Z. Gao, X. Shi, Z. Yang, X. Lin, H. Xu, J. D. Joannopoulos, M. Soljačić, H. Chen, L. Lu, Y. Chong, and B. Zhang, Nat. Commun. **7**, 11619 (2016).

[17] X. Cheng, C. Jouvaud, X. Ni, S. H. Mousavi, A. Z. Genack, and A. B. Khanikaev, Nat. Mater **15**, 542 (2016).

[18] T. Ma and G. Shvets, Phys. Rev. B **95**, 165102 (2017).

[19] J. B. Pendry, L. Martín-Moreno, and F. J. Garcia-Vidal, Science **305**, 847 (2004).

[20] D. Martin-Cano, M. L. Nesterov, A. I. Fernandez-Dominguez, F. J. Garcia-Vidal, L. Martin-Moreno, and E. Moreno, Opt. Express **18**, 754 (2010).

[21] X. Yin, Z. Ye, J. Rho, Y. Wang, and X. Zhang, Science **339**, 1405 (2013).

[22] J. Lu, C. Qiu, M. Ke, and Z. Liu, Phys. Rev. Lett. **116**, 093901 (2016).

[23] J. Lu, C. Qiu, L. Ye, X. Fan, M. Ke, F. Zhang, and Z. Liu, Nat. Phys. **13**, 369 (2017).

[24] L. Ye, C. Qiu, J. Lu, X. Wen, Y. Shen, M. Ke, F. Zhang, and Z. Liu, Phys. Rev. B **95**, 174106 (2017).

[25] Z. Gao, F. Gao, and B. Zhang, Appl. Phys. Lett. **108**, 041105 (2016).

[26] See Supplemental Material at http://link.aps.org/supplemental/10.1103/PhysRevB.96.201402 for measured photonic bandgap of the valley surface-wave photonic crystal.

[27] X. Wu, Y. Meng, J. Tian, Y. Huang, H. Xiang, D. Han, and W. Wen, arXiv:1703.04570.

[28] J. Noh, S. Huang, K. Chen, and M. C. Rechtsman, arXiv:1706.00059.

[29] F. Gao, H. Xue, Z. Yang, K. Lai, Y. Yu, X. Lin, Y. Chong, G. Shvets, and B. Zhang, arXiv:1706.04731.